PHYSICAL REVIEW B **98**, 195118 (2018)

Tuning the magnetic ground state of $Ce_{1-x}Yb_xRhIn_5$ by Yb valence fluctuations

S. Jang,[1,2,*] N. Pouse,[2,3] T. Keiber,[2,3] B. D. White,[2,3,†] S. M. Disseler,[4] J. W. Lynn,[4] J. C. Collini,[5,6] M. Janoschek,[2,3,7]
F. Bridges,[8] and M. B. Maple[1,2,3,‡]
[1]*Materials Science and Engineering Program, University of California, San Diego, La Jolla, California 92093, USA*
[2]*Center for Advanced Nanoscience, University of California, San Diego, La Jolla, California 92093, USA*
[3]*Department of Physics, University of California, San Diego, La Jolla, California 92093, USA*
[4]*NIST Center for Neutron Research, Gaithersburg, Maryland 20899, USA*
[5]*School of Physics and Astronomy, Rochester Institute of Technology, Rochester, New York 14623, USA*
[6]*Department of Physics, University of Maryland, College Park, Maryland 20742, USA*
[7]*MPA-CMMS Los Alamos National Laboratory, Los Alamos, New Mexico 87545, USA*
[8]*Department of Physics, University of California, Santa Cruz, California 95064, USA*

(Received 5 July 2018; revised manuscript received 10 October 2018; published 16 November 2018)

We characterize the properties of $Ce_{1-x}Yb_xRhIn_5$ single crystals with $0 \leqslant x \leqslant 1$ using measurements of powder x-ray diffraction, energy dispersive x-ray spectroscopy, electrical resistivity, magnetic susceptibility, specific heat, x-ray absorption near edge structure (XANES), and neutron diffraction. The Yb valence v_{Yb}, calculated from the magnetic susceptibility and measured using XANES, decreases from 3+ at $x = 0$ to ~2.1+ at $x_{\mathrm{act}} = 0.2$, where x_{act} is the measured Yb concentration. A transition from incommensurate to commensurate antiferromagnetism is observed in neutron diffraction measurements along $Q = (0.5, 0.5, l)$ between $0.2 \leqslant x_{\mathrm{act}} \leqslant 0.27$; this narrative is supported by specific-heat measurements in which a second robust feature appears at a temperature T_I ($T_I < T_N$) for the same concentration range. Magnetic susceptibility measurements also reveal features which provide additional evidence of magnetic ordering. The results of this study suggest that the evolution of the Yb valence plays a critical role in tuning the magnetic ground state of $Ce_{1-x}Yb_xRhIn_5$.

DOI: 10.1103/PhysRevB.98.195118

I. INTRODUCTION

Numerous studies on Ce-based heavy-fermion compounds, notably the CeMIn$_5$ (M = Co, Rh, Ir) family of compounds, have demonstrated the crucial role played by $4f$ electrons in unconventional superconductivity (SC), magnetic order, quantum criticality, and valence fluctuations [1–4]. The compound CeRhIn$_5$ is an ideal system in which to study the coexistence between magnetism and SC. Its temperature-pressure (T-P) phase diagram shows antiferromagnetic (AFM) ordering below a Néel temperature $T_N = 3.8$ K at ambient pressure, with T_N being suppressed to a quantum critical point as pressure is applied at a critical pressure $P_c = 2.25$ GPa. Near P_c, a broad dome of unconventional superconductivity with a maximum superconducting critical temperature of $T_c = 2.2$ K is found. The compound CeRhIn$_5$ is a relatively rare case in which the characteristic temperatures T_N and T_c are of the same magnitude, indicating a robust competition between antiferromagnetism and superconductivity [5–9].

Neutron diffraction experiments on CeRhIn$_5$ in zero applied magnetic field revealed that the antiferromagnetic ground state consists of antiferromagnetically coupled spin spirals that propagate along the c axis as characterized by propagation vector $q_M = (0.5, 0.5, 0.297)$ in terms of the reciprocal lattice units $2\pi/a$, $2\pi/b$, $2\pi/c$ (r.l.u.) and with Ce ion magnetic moments that reside within the tetragonal basal plane [6,10]. Neutron spectroscopy further demonstrated that this complex spiral ground state is a consequence of frustrated nearest- and next-nearest-neighbor exchange interactions along the c axis [11]. A spin-flop transition is observed when an external magnetic field of $\mu_0 H = 2$ T is applied within the ab plane [6,12]. Here, the magnetic field induces a surprisingly large easy-axis magnetic anisotropy that together with frustrated exchange interactions results in a rich low magnetic field phase diagram that can be explained by a model related to the axial next-nearest-neighbor Ising (ANNNI) model [13]. At low temperatures $T < T_1$ the field-induced easy-axis anisotropy results in a commensurate, "$++--$" magnetic structure, where the magnetic moments lying in the ab plane follow an up-up-down-down periodicity along the c axis [6,13]. A third, incommensurate magnetic phase is observed in the region $T_1 < T < T_N$, where the effect of the anisotropy is softened due to magnetic fluctuations arising near T_N. This results in an elliptical spin spiral with modulated magnetic moments that are predominantly oriented along the easy axis but exhibit small components perpendicular to it [6]. In agreement with the ANNNI model the propagation vector of the elliptical phase is strongly temperature dependent [13]. A study at higher magnetic fields uncovered evidence for nematic ordering similar to what is observed in iron-based

---

[*] Present address: Department of Physics, University of California, Berkeley, California 94720.

[†] Present address: Department of Physics, Central Washington University, 400 East University Way, Ellensburg, Washington 98926-7442.

[‡] Corresponding author: mbmaple@ucsd.edu

superconductors [14]. These recent studies suggest that the magnetic order in $\mathrm{CeRhIn_5}$ is highly tunable and here we explore this in more detail by means of Yb substitution on the Ce site.

The striking effects of Yb substitution on the physical properties of the heavy-fermion superconductor $\mathrm{CeCoIn_5}$, which have been reported in detail [15–19], motivated us to study the related system $\mathrm{Ce_{1-x}Yb_xRhIn_5}$. One interesting materials science issue encountered in the $\mathrm{Ce_{1-x}Yb_xCoIn_5}$ system is the discrepancy between the nominal Yb concentration x_{nom} and the actual Yb concentration x_{act} of the flux-grown single crystals; this issue is discussed in Refs. [20,21]. While the Ce valence remains stable at 3+ for all x in the $\mathrm{Ce_{1-x}Yb_xCoIn_5}$ system, the Yb valence decreases from 3+ to 2.3+ near $x_{\mathrm{nom}} = 0.2$ [22]. At the critical concentration of $x_{\mathrm{nom}} = 0.2$ where the Yb valence stabilizes, various unusual phenomena emerge. At this Yb concentration, the Fermi surface undergoes a reconstruction [23] and the quantum critical field H_{QCP} is suppressed [24]. There is also evidence from London penetration depth measurements that the nodal superconducting energy gap of $\mathrm{CeCoIn_5}$ crosses over to a nodeless gap at this Yb concentration [25]; on the other hand, recent thermal conductivity measurements are consistent with a robust nodal superconducting energy gap for all Yb concentrations [26]. Identifying the symmetry of the superconducting order parameter remains an interesting and unresolved issue in the system $\mathrm{Ce_{1-x}Yb_xCoIn_5}$.

In this paper, we report the results of powder x-ray diffraction (XRD), energy dispersive x-ray spectroscopy (EDS), electrical resistivity, magnetization, specific heat, and neutron diffraction measurements on the $\mathrm{Ce_{1-x}Yb_xRhIn_5}$ system; these measurements reveal many similarities with the $\mathrm{Ce_{1-x}Yb_xCoIn_5}$ system. The unit-cell volume vs x exhibits an analogous deviation from Vegard's law, demonstrating a discrepancy between Yb concentrations x_{act} and x_{nom}. The Yb valence, which is determined through multiple experimental techniques, is found to change from 3+ to 2.1+ near $x_{\mathrm{act}} \approx 0.2$. Neutron diffraction measurements show that there is also a crossover from an incommensurate to a commensurate magnetic structure near this Yb concentration. Furthermore, a second feature, presumably of magnetic origin, emerges in specific-heat measurements for samples with $x_{\mathrm{act}} \geqslant 0.18$. These and other observations hint at a potential relationship between the magnetic ground state in $\mathrm{Ce_{1-x}Yb_xRhIn_5}$ and the valence of Yb. Since the discrepancy in Yb concentration of $\mathrm{Ce_{1-x}Yb_xRhIn_5}$ single crystals is qualitatively identical to that of $\mathrm{Ce_{1-x}Yb_xCoIn_5}$ and thoroughly explained in the paper of Jang *et al.* [21], all of the references to Yb concentration x in this paper represent the actual Yb concentration ($x = x_{\mathrm{act}}$).

II. EXPERIMENTAL DETAILS

Single-crystalline samples of $\mathrm{Ce_{1-x}Yb_xRhIn_5}$ were grown using a molten indium flux method [27]. For concentrations $x_{\mathrm{nom}} > 0.9$, heat treatment at significantly higher temperature ($T > 1300\,^{\circ}\mathrm{C}$) is required with the elements sealed in a metallic crucible, such as a Ta or Mo tube, as opposed to quartz in order to successfully grow the crystals [28]. Since our laboratory did not have access to these temperatures or metallic crucibles, we attempted to grow these Yb-rich compounds with $T < 1200\,^{\circ}\mathrm{C}$ in a quartz crucible. This resulted in an inability to form high-quality single crystals with $0.28 \leqslant x_{\mathrm{act}} \leqslant 1$. Additionally, the reported discrepancies in the Yb concentration could be attributed to this difficulty in synthesizing crystals with higher Yb concentrations due to the lower than ideal melting temperatures in conjunction with the potential for the Yb to react with the excess In to form the binary compound $\mathrm{YbIn_3}$. For these reasons, we were unable to perform reliable measurements, including neutron scattering, on single crystals of $\mathrm{Ce_{1-x}Yb_xRhIn_5}$ for $0.28 \leqslant x_{\mathrm{act}} \leqslant 1$. Polycrystalline ingots of $\mathrm{Ce_{1-x}Yb_xRhIn_5}$ were formed using traditional arc-melting techniques for selected Yb concentrations. X-ray diffraction (XRD) measurements were performed on powdered single crystals in a Bruker D8 Discover x-ray powder diffractometer using a Cu-K_α source to characterize the crystal structure. Analysis of chemical compositions was performed through transmission x-ray spectroscopy (TXAS) and energy dispersive x-ray spectroscopy (EDS) measurements, as described previously [21].

Magnetic susceptibility measurements were performed between 300 and 2 K using a magnetic property measurement system (MPMS) equipped with a 7-T superconducting magnet from quantum design (QD). Four-wire electrical resistivity measurements were performed from 300 K down to ~1.1 K in a pumped ^{4}He Dewar. Specific-heat measurements were performed down to 1.8 K in a QD physical property measurement system (PPMS) DynaCool using a standard thermal relaxation technique. Extended x-ray absorption fine structure (EXAFS) measurements were collected on powdered samples at the SLAC National Accelerator Laboratory on beamline 4-1. Transmission spectroscopy measurements were performed on the Ce and Yb L_{III} edges and on the Rh K edge.

Neutron diffraction measurements were made on BT-4 and BT-7 triple-axis spectrometers at the NIST Center for Neutron Research (NCNR) [29]. Single crystals were mounted in the *HHL* scattering plane and measured with neutrons of incident energy $E_i = 14.7$ meV ($\lambda = 2.359$ Å). Coarse collimations of open 80'-80'-120' or 40'-40'-40'-open full width at half-maximum (FWHM) were used on BT-7 and BT-4, respectively, while 10'-10'-40' and open-50'-40'-radial were used for the high-resolution diffraction with the position sensitive detector on BT-7. Measurements were performed either in a helium cryostat with a base temperature of 1.5 K, or a He^3 system with a base temperature of 0.3 K.

III. RESULTS AND DISCUSSION

A. X-ray diffraction

The crystal structure of $\mathrm{Ce_{1-x}Yb_xRhIn_5}$ is tetragonal with space group $P4/mmm$ for all temperatures below 300 K and for all x values. Rietveld refinements were performed on several XRD patterns using GSAS [30] and EXPGUI [31]. In Fig. 1, the powder XRD pattern for a representative sample is shown. The Rietveld refinement is plotted in red and the measured XRD data are plotted as a black curve. We obtained good agreement between the measured XRD pattern and the refinement calculations for the expected crystal structure, which is quantified by reduced χ^2 values of less than 3 for most concentrations, but with some deviation when x is large.

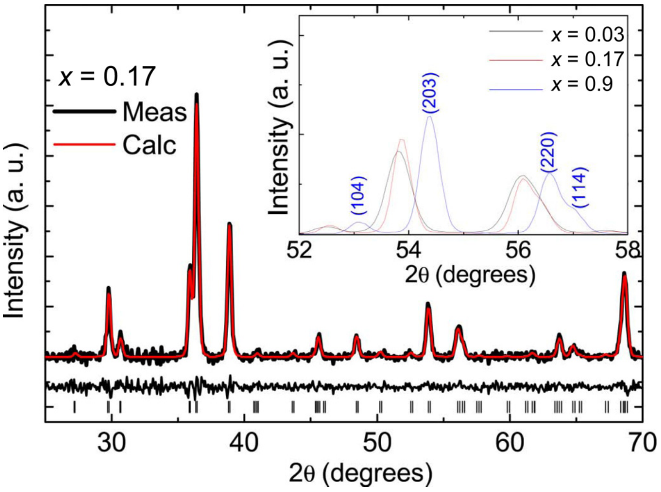

FIG. 1. A representative XRD pattern for the $x = 0.17$ sample is plotted. The expected Bragg peak positions are indicated with small ticks above the labeled 2θ axis. The calculated fit from Rietveld refinement is plotted as the top (red) curve and the deviation from the fit is shown as the bottom (black) curve above the Bragg peak indicators. The inset illustrates differences in the XRD patterns for different Yb concentrations over a narrow window of 2θ. The peaks shift slightly between $x = 0.03$ and 0.17, and then shift significantly for $x = 0.9$.

The inset of Fig. 1 illustrates the shift in Bragg-peak positions as x increases, indicating systematic changes in the lattice parameters. Using the Rietveld refinement technique, lattice parameters a and c were determined and are plotted along with the calculated unit-cell volume in Fig. 2.

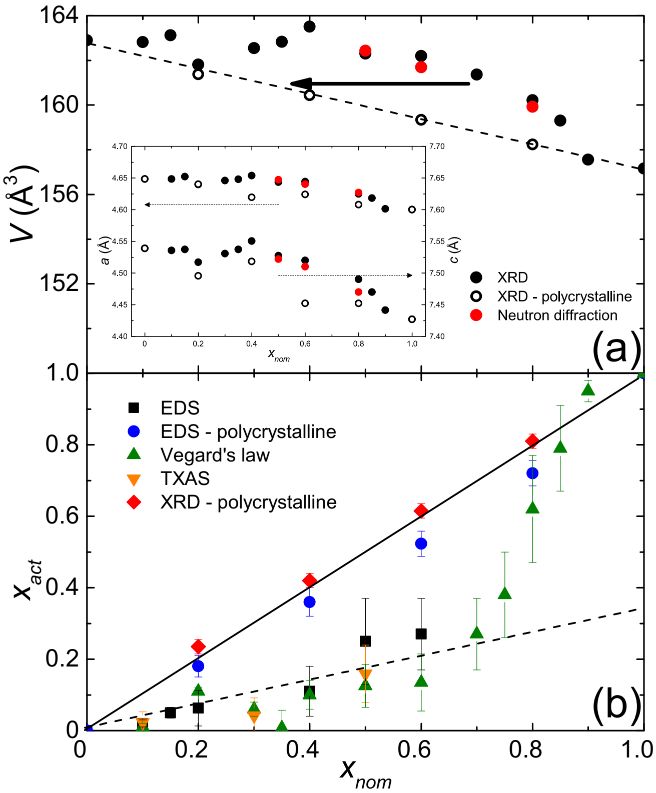

FIG. 2. (a) Unit-cell volumes, plotted as a function of x_{nom}, calculated from XRD and neutron diffraction measurements on single-crystal and polycrystalline samples. A linear extrapolation representing Vegard's law between the two parent compounds is shown as a guide to the eye; the horizontal (black) arrow emphasizes the discrepancy between the measured behavior of $V(x)$ and the Vegard's law construction. Plotted in the inset are the lattice parameters a and c vs x_{nom}. (b) Comparison between the nominal and actual Yb concentrations determined from EDS, TXAS, and XRD measurements. A dashed line is drawn with slope $x_{\mathrm{act}} = x_{\mathrm{nom}}/3$, which fits the single-crystal data well for concentrations $x_{\mathrm{nom}} < 0.7$. For higher concentrations, the data deviate from this line and approach the $x_{\mathrm{act}} = x_{\mathrm{nom}}$ line. The results from EDS and XRD measurements on polycrystalline samples fit the expected relation shown by the line $x_{\mathrm{act}} = x_{\mathrm{nom}}$. Error bars where indicated represent one standard deviation throughout the paper. These analyses establish a relationship between x_{act} and x_{nom}, ensuring that all subsequent discussions of Yb concentration can be limited to the actual concentration, such that $x = x_{\mathrm{act}}$, unless otherwise stated.

Single crystals of $\mathrm{Ce}_{1-x}\mathrm{Yb}_x\mathrm{CoIn}_5$, synthesized using an indium flux technique, are well-known to have a sub-nominal Yb concentration. As part of this study, we found that our $\mathrm{Ce}_{1-x}\mathrm{Yb}_x\mathrm{RhIn}_5$ single crystals also contain a subnominal Yb concentration. To address this issue in the Rh system, we compare the results from XRD, EDS, TXAS, and neutron diffraction measurements in Fig. 2. The initial indication of the discrepancy between the nominal Yb concentration x_{nom} and the actual Yb concentration x_{act} comes from unit-cell volume data, where a deviation from Vegard's law is shown in Fig. 2(a). Since the valences of Ce and Yb are known to be constant from supporting measurements of XAFS and magnetic susceptibility for $x > 0.2$, the deviation from Vegard's law can be explained by a discrepancy between x_{act} and x_{nom}; this is resolved by shifting unit-cell volume data so that it coincides with the linear extrapolation of Vegard's law and defining the resulting x value as the actual concentration of Yb, x_{act}. When x_{act} is plotted as a function of x_{nom} in Fig. 2(b), we see a relationship between the two concentrations which can be represented by the equation $x_{\mathrm{act}} = x_{\mathrm{nom}}/3$ up to about $x_{\mathrm{nom}} = 0.7$. There is a sharp deviation from this behavior over a narrow concentration range between $0.7 \leqslant x_{\mathrm{nom}} \leqslant 0.85$ before Vegard's law ($x_{\mathrm{act}} = x_{\mathrm{nom}}$) is obeyed for $x_{\mathrm{nom}} \geqslant 0.9$. The conclusions drawn from this application of Vegard's law are supported by EDS and TXAS measurements on the single crystals, which are also shown in Fig. 2(b). This scenario is qualitatively identical to that of the Co series, which is discussed in the paper of Jang *et al.* [21]. We found that polycrystalline samples of $\mathrm{Ce}_{1-x}\mathrm{Yb}_x\mathrm{RhIn}_5$, which were also studied using XRD and EDS measurements, show an agreement between x_{nom} and x_{act}; the discrepancy, therefore, appears to be limited by the solubility of Yb in Ce for the temperature range (room temperature $\leqslant T \leqslant 1200\,^\circ\mathrm{C}$) covered in our flux growth technique. With the relationship between actual and nominal concentrations of Yb being well established, all mentions of Yb concentration x for $\mathrm{Ce}_{1-x}\mathrm{Yb}_x\mathrm{RhIn}_5$ hereafter refer to the actual concentration of Yb ($x = x_{\mathrm{act}}$) in this paper.

B. XANES

The step height in the absorption edge in transmission x-ray spectroscopy (TXAS) is a direct measurement of the

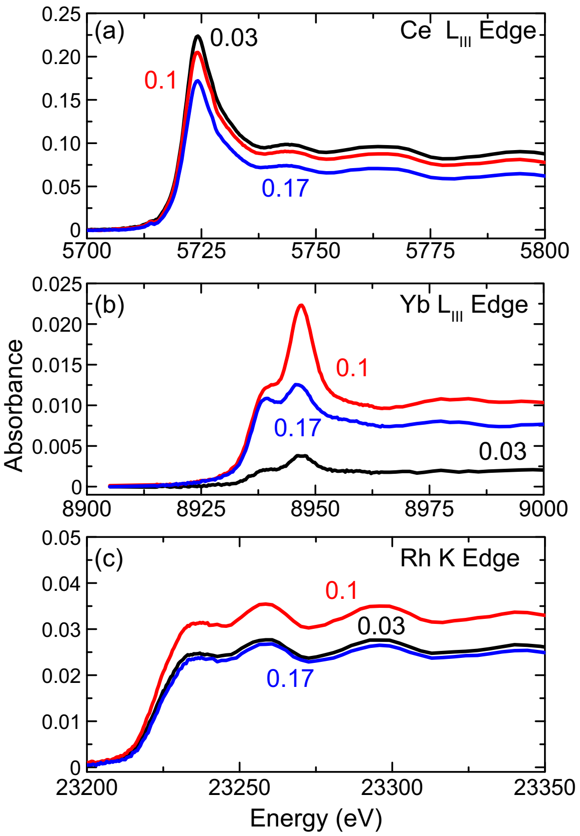

FIG. 3. Un-normalized XANES data for Yb, Ce, and Rh. (a) Shows the Ce $L_{\rm III}$ XANES for Ce$_{1-x}$Yb$_x$RhIn$_5$ where $x = 0.03$ is the top black line, followed by $x = 0.1$ as the red intermediate line, and $x = 0.17$ as the lower blue line. (b) The Yb $L_{\rm III}$ XANES, and (c) the Rh K XANES are shown for the same concentrations. All data were collected at $T = 200$ K and the "pre-edge" has been subtracted from the data.

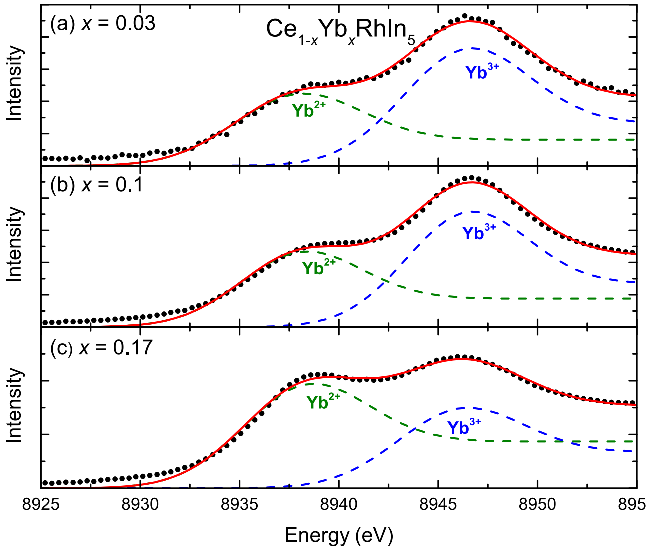

FIG. 4. Measured Yb $L_{\rm III}$ edge data for Ce$_{1-x}$Yb$_x$RhIn$_5$ are plotted as black circles. The fit to the two-edge model is shown as the red solid line, while the dashed green line represents the contribution from Yb^{2+}, and the dashed blue line represents the contribution from Yb^{3+}. The results are shown over the same energy ranges for $x =$ 0.03, 0.1, and 0.17 in panels (a), (b), and (c), respectively.

number of atoms in the unfocused x-ray beam. Consequently, the ratio of the edge step heights for different elements in a sample, keeping the illuminated region of the sample the same for each edge energy, provides a measure of the relative concentrations. To get actual concentration ratios, each edge step height must be divided by the absorption cross-sectional area for that element [32]. The absorption edge step height was determined by a simple linear construction technique above and below the edge. We have used this approach recently to determine concentration ratios in the Ce$_{1-x}$Yb$_x$CoIn$_5$ system [21] and use a similar approach here. For such measurements, thin layers of powdered material were used to minimize the effects of pinholes, inclusions of indium flux, and to prevent saturation effects.

The XANES for Ce $L_{\rm III}$, Yb $L_{\rm III}$, and Rh K edges are shown in Figs. 3(a), 3(b), and 3(c) for the $x = 0.03$, 0.1, and 0.17 samples, respectively. The ratio of the In (edge not shown) concentration to the Rh concentration was roughly 4.8 ± 0.2 for each of the three concentrations measured, indicating that the Rh site is nearly fully occupied. The occupation of the Ce $L_{\rm III}$ and Yb $L_{\rm III}$ edges was determined by comparing the aforementioned cross section adjusted edge height ratios to the Rh K edge for the same concentration. These results are presented in Fig. 2(b) for Yb for comparison with EDS and XRD measurements.

The Ce $L_{\rm III}$ edge and Rh K edge exhibit only a single-edge feature which indicates that only a single valence state is present for these atoms in the material. In contrast, the Yb $L_{\rm III}$ edge, shown in detail in Fig. 4, is composed of two slightly offset edges, indicating a mixed valence state. We briefly describe the XANES analysis used to determine the valence states for the different concentrations. The Yb^{2+} and Yb^{3+} valence states have different edge energies which are offset by several eV; Yb^{2+} absorbs near 8938 eV and Yb^{3+} near 8946 eV. To quantitatively determine the valence, two different offset edges were fit to the XANES data. Each edge is a sum of a broadened step function plus a Gaussian peak, centered at the same energy; the edge step is modeled as a convolution of a Gaussian distribution with a unit step function, and all Gaussians are assumed to have the same width σ. The relative amplitudes of the Gaussians, the locations of each edge E_1 and E_2, σ, and relative step heights were all determined from nonlinear fits for each concentration. The fit was conducted only in the immediate vicinity of the edges where additional features of the XANES edge are minimal compared with the first, large peaks. In a recent XANES study of CaF$_2$:Yb, the absorption matrix element for the 2+ valence was found to be about 7% lower than for the 3+ valence state [33]. This correction was included in estimating the fractions $p_{\rm Yb^{2+}}$ and $p_{\rm Yb^{3+}}$ of the 2+ and 3+ valences, respectively. Then, the Yb average valence z is given by $z = 2p_{\rm Yb^{2+}} + 3p_{\rm Yb^{3+}}$. These measurements show that the substituted Yb ion shifts from nearly trivalent Yb^{3+} at $x = 0$ down to intermediate-valence Yb$^{2.1+}$ by $x = 0.2$.

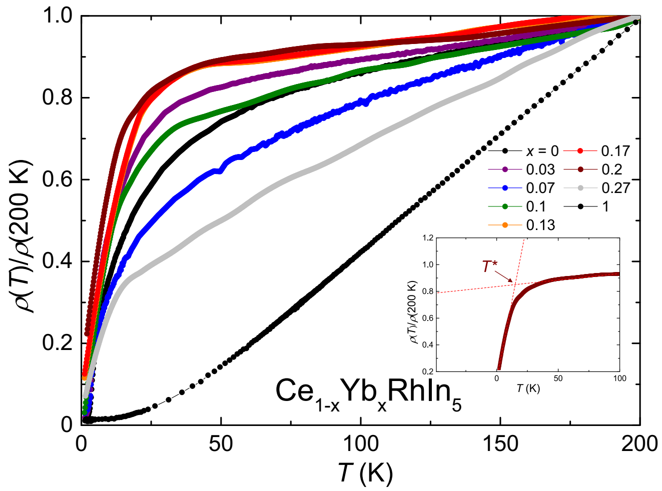

FIG. 5. Electrical resistivity data for selected samples of $\mathrm{Ce}_{1-x}\mathrm{Yb}_x\mathrm{RhIn}_5$, normalized by electrical resistivity values measured at 200 K. The Kondo coherence feature for samples is observed near 25 K. (Inset) Example of T^* being calculated for the $x = 0.2$ sample.

C. Electrical resistivity

Electrical resistivity measurements were performed on selected $\mathrm{Ce}_{1-x}\mathrm{Yb}_x\mathrm{RhIn}_5$ samples. These data are plotted in Fig. 5 and show an evolution of the Kondo lattice with Yb concentration in the range $0 \leqslant x \leqslant 0.27$. We observe a coherence peak associated with the Kondo lattice behavior which is manifested as a kneelike feature.

In Fig. 6, the Kondo coherence temperature T^* and $\rho(T^*)/\rho(200\text{ K})$ are plotted as a function of x. We defined T^* as the temperature where the slope of the resistivity exhibits the largest change; an example of this procedure is provided in the inset of Fig. 5. Values for T^* and $\rho(T^*)/\rho(200\text{ K})$ remain relatively stable with a slight dip as x increases from 0 to 0.2, before being rapidly suppressed as the Kondo lattice loses coherence at higher values of x; this coincides with the concentration where the Yb valence stabilizes at $v_{\mathrm{Yb}} = 2.1+$. The stability of the Kondo lattice in the region $x < 0.2$ may suggest a cooperative relationship between a decreasing, unstable Yb valence and the decrease in number of host Ce^{3+} ions with increasing x. Once the Yb valence becomes stable at about 2.1+, the Kondo lattice behavior weakens as Ce is replaced by Yb. This x-dependent behavior of the Kondo lattice is consistent with other findings in the $\mathrm{Ce}_{1-x}\mathrm{Yb}_x\mathrm{RhIn}_5$ system where the valence of Yb and the magnetic structure are intertwined.

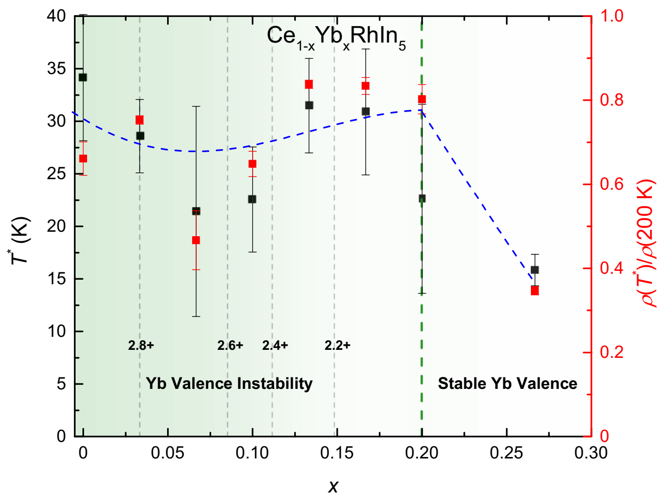

FIG. 6. The characteristic Kondo coherence temperature T^* and $\rho(T^*)/\rho(200\text{ K})$ vs Yb concentration x. The Yb valence is indicated by the false (color) background (3+ on the green side at $x = 0$ and $\sim 2.1+$ for $x > 0.2$). The Yb valence crossover at $x = 0.2$ is indicated by a vertical dashed (green) line that acts as a guide to the eye. A blue dashed curve shows the progression of both T^* and $\rho(T^*)/\rho(200\text{ K})$ as a function of x.

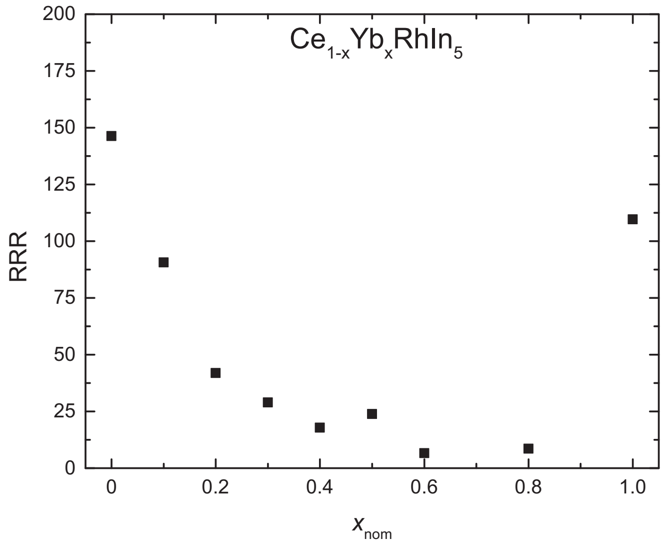

FIG. 7. Calculated RRR values from $\rho(T)$ plotted vs x_{nom} for $\mathrm{Ce}_{1-x}\mathrm{Yb}_x\mathrm{RhIn}_5$. At $x_{\mathrm{nom}} = 0$, the RRR ≈ 150. As Yb is introduced, the RRR drops precipitously. For the pure YbRhIn_5 compound, the RRR increases to above 110, suggesting that substituted samples are likely to yield low RRR values, potentially related to the issues raised regarding synthesis in the range $x_{\mathrm{nom}} > 0.8$ discussed in the text.

For the samples whose measurements are presented in Figs. 5 and 6, the residual resistivity ratio (RRR) was calculated according to the relation

$$\mathrm{RRR} = \rho(300\text{ K})/\rho(0\text{ K}), \tag{1}$$

where the values of $\rho(0\text{ K})$ were estimated by extrapolating the $\rho(T)$ data to 0 K. The RRR values for the nominal Yb concentration range $0 \leqslant x_{\mathrm{nom}} \leqslant 1$ are plotted in Fig. 7. The evolution of the RRR with x_{nom} shows significantly large values of the RRR for both parent compounds ($x = 0$ and 1). However, as x_{nom} is increased from 0, the RRR drops precipitously, which suggests a possible relationship between the RRR and the difficulty in synthesizing substituted samples of $\mathrm{Ce}_{1-x}\mathrm{Yb}_x\mathrm{RhIn}_5$ (described in Sec. II).

D. Magnetic susceptibility

Measurements of magnetic susceptibility as a function of temperature were made with the magnetic field H oriented both in the ab plane and along the c axis; the measured

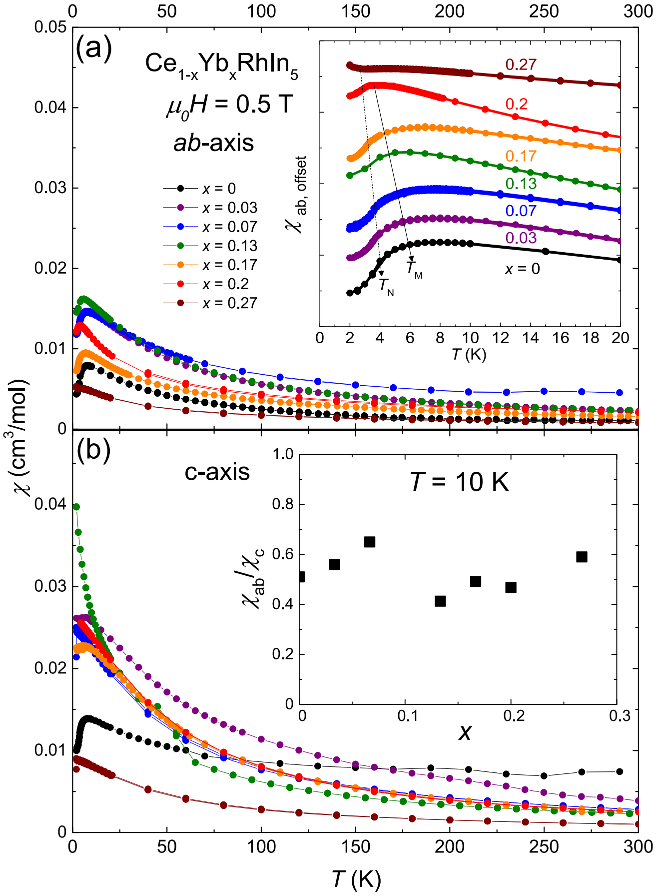

FIG. 8. (a) Magnetic susceptibility measured in an applied magnetic field of $\mu_0 H = 0.5$ T along the *ab* plane is plotted from 0 to 300 K. The inset shows data for $0 \leqslant T \leqslant 20$ K where a black, dotted line is drawn through an inflection point, which is a signature of the AFM transition. The maximum value of magnetic susceptibility decreases with x. The temperature of the maximum is denoted T_M and is shown by the dashed-dotted line. Due to a low-T upturn in the magnetic susceptibility for $x = 0.27$, T_N is difficult to define, and thus not indicated with the dashed line. (b) Magnetic susceptibility data measured with magnetic field applied along the c axis are plotted from 0 to 300 K. For this orientation, only some concentrations exhibit a clear feature at low temperature associated with AFM ordering; other concentrations are dominated by an upturn in this temperature range. The inset shows the ratio χ_{ab}/χ_c at 10 K, which is above the AFM transition but below the temperature range exhibiting Curie-Weiss behavior. The values of χ_{ab}/χ_c are scattered about 0.5 over the range of concentrations measured.

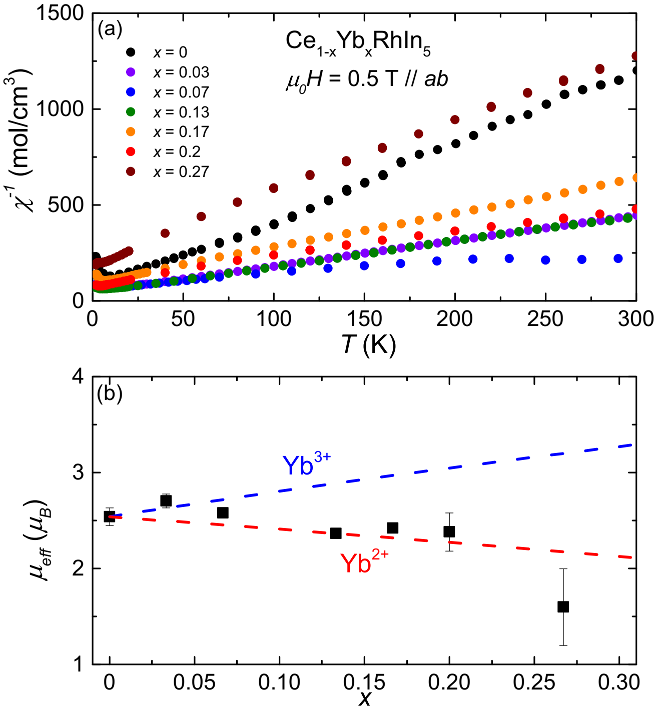

FIG. 9. (a) Inverse magnetic susceptibility χ_{ab}^{-1}, plotted for temperatures up to 300 K, exhibits linear Curie-Weiss behavior at high temperatures. (b) The effective magnetic moment $\mu_{\rm eff}$ for $x < 0.33$ was calculated from the c-axis measurements and is plotted as a function of x. Dashed curves indicate theoretical calculations for $\mu_{\rm eff}$ in Ce$_{1-x}$Yb$_x$RhIn$_5$ assuming Yb valences of Yb^{2+} and Yb^{3+}.

magnetization M was divided by the applied magnetic field $\mu_0 H = 0.5$ T to obtain the magnetic susceptibility. These data are plotted as a function of temperature in Fig. 8. Two features are apparent in the data at low temperature, which are highlighted in the inset of Fig. 8(a). The inflection point, which is the signature for the AFM transition, is indicated by a dotted black line that acts as a guide to the eye. The maximum value of the magnetic susceptibility is observed at a temperature T_M that decreases with increasing x. This maximum at T_M corresponds to a deviation from Curie-Weiss behavior and is consistent with the crystalline electric field effects observed in CeRhIn$_5$ [34,35]. The inset of Fig. 8(b) shows the ratio of magnetic susceptibility with magnetic field applied in both orientations at 10 K. The ratio is roughly constant at $\chi_{ab}/\chi_c = 0.5$ for $x < 0.3$.

The inverse of the magnetic susceptibility χ^{-1} vs T is plotted over a large temperature range in Fig. 9(a). For all x, the $\chi(T)$ data can be described by the Curie-Weiss relation

$$M/H = C_0/(T - \Theta_{\rm CW}), \tag{2}$$

where C_0 is the Curie constant and $\Theta_{\rm CW}$ is the Curie-Weiss temperature. The average effective magnetic moment of the rare-earth ions, $\mu_{\rm eff}$, is estimated using the relation $C_0 = \mu_{\rm eff}^2 N_A/3k_B$, where N_A is Avogadro's number and k_B is Boltzmann's constant.

Values of $\mu_{\rm eff}(x)$ are found to decrease monotonically from $\sim 2.5\,\mu_B$ for $x = 0$ to approximately $1.6\,\mu_B$ at $x = 0.27$. To obtain an estimate for the valence of Yb, $\upsilon_{\rm Yb}$, data for $\mu_{\rm eff}(x)$ can be modeled using the equation

$$\mu_{\rm eff} = \sqrt{(\mu_{\rm Ce^{3+}})^2(1-x) + \{(\mu_{\rm Yb^{3+}})^2[\upsilon_{\rm Yb}(x) - 2](x)\}}, \tag{3}$$

where the free-ion values of $\mu_{\rm Ce^{3+}}$ and $\mu_{\rm Yb^{3+}}$ are 2.54 and 4.54 μ_B, respectively, and $\upsilon_{\rm Yb}$ represents the valence of Yb.

Values of $\mu_{\rm eff}$ are plotted in Fig. 9(b) as a function of x. The dashed lines represent the theoretical behavior for $\mu_{\rm eff}(x)$ using Eq. (3) and assuming that all Yb ions are either divalent or trivalent. In these calculations, Ce is always assumed to be trivalent. We observe that $\mu_{\rm eff}(x)$ follows the behavior

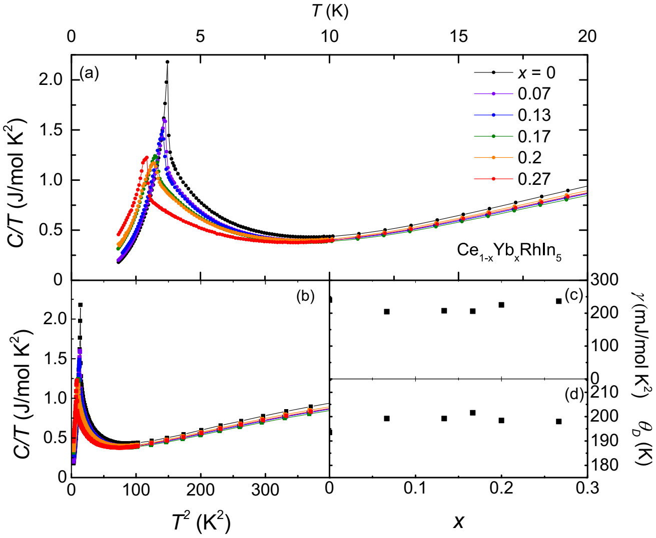

FIG. 10. (a) Specific heat divided by temperature C/T, plotted as a function of temperature T. (b) C/T plotted as a function of T^2 for selected concentrations; the linear region of data in the temperature range $T > T_N$ obeys the relationship $C/T \simeq \gamma + \beta T^2$. Best-fit results are plotted as functions of actual Yb concentration x_{act} for (c) the Sommerfeld coefficient γ and (d) the Debye temperature Θ_D.

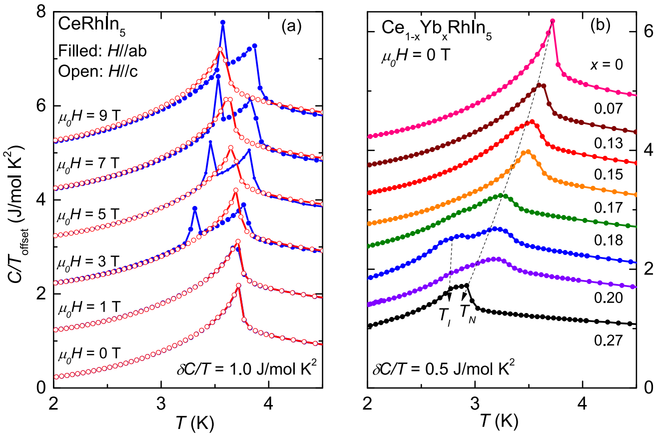

FIG. 11. (a) Specific heat divided by temperature C/T for CeRhIn$_5$ in applied magnetic fields $\mu_0 H$ of up to 9 T; H was applied parallel to both the ab plane (filled circles) and along the c axis (open circles). Note that data measured in different magnetic fields have been offset from one another by an amount $\delta C/T = 1.0$ J/mol K^2 for visual clarity. When $H \parallel c$, we observe a single feature at T_N which is gradually suppressed to lower temperature with increasing H. When $H \parallel ab$ and $\mu_0 H > 3$ T, we observe a feature at T_N and a magnetic-field-induced phase transition at T_1 ($T_1 < T_N$). (b) C/T data for Ce$_{1-x}$Yb$_x$RhIn$_5$ are plotted in the vicinity of T_N. The data for different concentrations have been offset from one another by an amount $\delta C/T = 0.5$ J mol/K^2 for visual clarity. A second feature emerges at temperatures $T_I < T_N$ for $x_{\mathrm{act}} > 0.18$. Dashed lines are guides to the eye which emphasize the evolution of T_N and T_I with Yb concentration.

expected for Yb^{3+} for very low x until it crosses over to being more consistent with Yb^{2+}. This result is consistent with the study of Ce$_{1-x}$Yb$_x$CoIn$_5$ where Yb is trivalent near $x = 0$, but its valence decreases to an intermediate value of 2.3+ at $x \approx 0.07$ [22]. We applied Eq. (3) to extract values for v_{Yb} as a function of x; the values obtained are consistent with results from TXAS measurements as described in the discussion section.

E. Specific heat

Specific-heat measurements were performed in zero magnetic field on samples in the system Ce$_{1-x}$Yb$_x$RhIn$_5$ with actual Yb concentrations of $x_{\mathrm{act}} = 0$, 0.07, 0.13, 0.15, 0.17, 0.18, 0.2, 0.23, and 0.27. These data are displayed in Fig. 10(a) with C/T plotted as a function of temperature below 20 K. A dramatic evolution of the magnetic phase transition with Yb concentration is evident both in the suppression of T_N and in the change in magnitude of the feature at T_N. These results are consistent with a similar evolution with x that was observed in the systems Ce$_{1-x}$La$_x$RhIn$_5$ and Ce$_{1-x}$Y$_x$RhIn$_5$ [27,36]. The magnitude of the peak at T_N decreases with increasing x as a broad hump feature emerges near T_N. This broad hump is a signature of short-range magnetic correlations that take an increasing amount of the entropy, leaving a smaller peak feature with less entropy at T_N [36].

The Sommerfeld coefficient γ and Debye temperature Θ_D were determined from these data by plotting C/T vs T^2 and fitting the linear portion for $T > T_N$ with the expression $C/T \simeq \gamma + \beta T^2$, where $\beta = \frac{12\pi^4 N_A k_B}{5\Theta_D^3}$. Such a procedure is shown for representative data in Fig. 10(b), where a linear region is seen for $T > T_N$. The best-fit results for γ and Θ_D are plotted as functions of x in Figs. 10(c) and 10(d), respectively. The Sommerfeld coefficient for most Yb concentrations is roughly $\gamma \approx 200$ mJ mol^{-1} K^{-2}. γ was previously determined from low-temperature ($T < T_N$) fits to C/T data in two studies of the system Ce$_{1-x}$La$_x$RhIn$_5$ [36,37]; this procedure resulted in smaller values of γ: $\leqslant$100 mJ mol-Ce^{-1} K^{-2} and $\sim$50 mJ mol^{-1} K^{-2} [36,37]. Kim *et al.* discussed the difficulty of extracting γ from data for CeRhIn$_5$ because of the contributions due to magnetic order [37]. Our results for γ may be higher than previous results due to partial gapping of the Fermi surface that is associated with the formation of the spin density wave (SDW) ground state [10]. We extracted γ using data measured at $T > T_N$ where the Fermi surface is presumably ungapped, while Refs. [36,37] used fits to data in the temperature range $T < T_N$. The Debye temperature is relatively x independent, as expected, maintaining a value of $\Theta_D \simeq 200$ K for all Yb concentrations.

In zero magnetic field, the compound CeRhIn$_5$ exhibits an incommensurate antiferromagnetic structure below T_N, characterized by a wave vector $q_M = (\frac{1}{2}, \frac{1}{2}, 0.297)$ and Ce moments that reside within the easy ab plane [10]. When a magnetic field is applied within the ab plane, a field-induced phase transition is observed [6,12]. Such a transition has also been observed in measurements on the system Ce$_{1-x}$La$_x$RhIn$_5$ under similar conditions [36]. Below T_1, as field is applied, CeRhIn$_5$ enters the "+ + − −", commensurate magnetic phase [6]. Data from heat-capacity measurements on CeRhIn$_5$ in magnetic fields up to $\mu_0 H = 9$ T are shown in Fig. 11(a). A magnetic-field-induced feature at $T_1 < T_N$ is observed when $\mu_0 H \geqslant 3$ T and $H \parallel ab$, and T_N is observed to increase with increasing H. When $H \parallel c$, T_N is slowly suppressed

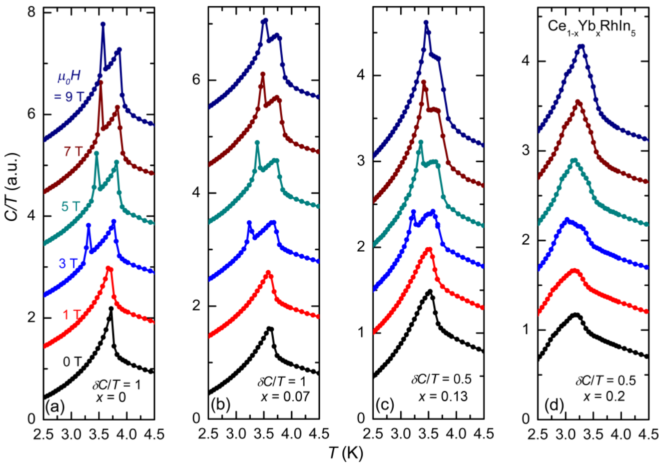

FIG. 12. Specific-heat divided by temperature C/T vs temperature T for selected Yb concentrations in the system $\mathrm{Ce}_{1-x}\mathrm{Yb}_x\mathrm{RhIn}_5$: (a) $x = 0$, (b) $x = 0.07$, (c) $x = 0.13$, and (d) $x = 0.20$. For each concentration, measurements were performed in applied magnetic fields of $\mu_0 H = 0$, 1, 3, 5, 7, and 9 T (applied along the ab plane). Data measured in different magnetic fields have been offset from one another by an amount $\delta C/T = 0.5$–1 J/mol K^2 for visual clarity. Two distinct features are observed in CeRhIn_5 for $\mu_0 H \geqslant 3$ T. At constant magnetic field, these features appear to merge with increasing x, such that a single broad feature is observed for $x = 0.20$ in magnetic fields of up to 9 T.

and it appears that no magnetic-field-induced features emerge. These results agree with those from previous reports [36].

Zero-field specific-heat measurements for $\mathrm{Ce}_{1-x}\mathrm{Yb}_x\mathrm{RhIn}_5$ single crystals are displayed in Fig. 11(b); these data have been offset by an amount $\delta C/T = 0.5$ J mol^{-1} K^{-2} for visual clarity. Yb substitution for Ce suppresses T_N at a rate that appears to be consistent with that for La and Y substitution [27,36,37]. On the other hand, unlike in previous work on La and Y substitution, we observe a second feature that emerges at a temperature $T_I < T_N$ for $x \geqslant 0.18$. T_I decreases slowly with increasing x. The character of this broad feature seems to preclude it from being associated with a first-order phase transition.

Specific-heat measurements were performed in the vicinity of the AFM transition for $\mathrm{Ce}_{1-x}\mathrm{Yb}_x\mathrm{RhIn}_5$ with $x_{\mathrm{act}} = 0, 0.07, 0.13, 0.20$ in applied magnetic fields up to $\mu_0 H = 9$ T. These results are summarized in Fig. 12. The data measured at different magnetic fields have been offset by amounts $\delta C/T$ to more clearly follow the evolution of behavior with H. A first-order magnetic-field-induced phase transition is observed for $x_{\mathrm{act}} = 0$, 0.07, and 0.13 when $\mu_0 H \geqslant 3$ T; we were unable to observe any strong signature of this magnetic-field-induced transition in data for $x_{\mathrm{act}} = 0.20$. It appears that the separation between T_1 and T_N decreases with increasing x, suggesting that disorder may promote a commensurate magnetic structure over the incommensurate magnetic structure of CeRhIn_5.

One explanation for the tendency towards commensurate magnetic order may be that disorder weakens the next-nearest-neighbor exchange interactions, thus lifting the magnetic frustration between antiferromagnetic nearest- (J_1) and next-nearest-neighbor (J_2) exchange along the c axis that drives the emergence of the incommensurate antiferromagnetic structure for $x_{\mathrm{act}} = 0$ [11]. Another possibility is that changes in the Yb valence as x is increased could affect the orbital characteristics of the $4f$ electronic wave function and, in turn, result in additional magnetic anisotropies that favor commensurate order. We note that such changes in orbital character have recently been reported both as a function of chemical substitution [38] and magnetic field [39]. Both T_1 and T_N increase with increasing H, which is consistent with the H-T phase diagram determined by Light *et al.* for the case of La substitution [36]. One possibility is for the two effects described above to work in tandem to generate the observed behavior. However, based on similarities to the $\mathrm{Ce}_{1-x}\mathrm{Yb}_x\mathrm{CoIn}_5$ system, which exhibits a valence transition at the same value of x where there is a change in the electronic structure, and the fact that the RRR is consistently large throughout the full range of x shown in Fig. 7, it seems more likely that the latter mechanism involving changes in the orbital characteristics of the $4f$ electronic wave functions causes the modifications in the magnetic structure.

F. Neutron diffraction

Neutron diffraction measurements, collected in the HHL scattering plane with neutrons of incident energy $E_i = 14.7$ meV, are able to probe the crystal structure, magnetic moments of the constituent ions, and the magnetic structure of the ordered ground states. We performed such measurements on our $\mathrm{Ce}_{1-x}\mathrm{Yb}_x\mathrm{RhIn}_5$ single crystals to determine whether or not there is a link between the variation of the Yb valence and the magnetic structure. To extract meaningful magnetic moments from neutron scattering data, corrections for neutron-neutron absorption must be made [40]. Due to the large neutron absorption cross sections of both In and Rh, and the irregular shape of the samples, making the corrections is problematic in the present case and, hence, the moment values from the magnetic susceptibility measurements are likely more reliable.

An incommensurate AFM structure was found for samples with $x = 0.17$ and 0.2 that could be described by a propagation vector $q = (0.5, 0.5, 0.297(0.002))$; this magnetic structure is identical to that of CeRhIn_5 [10]. The magnetic scattering intensity is obtained in terms of absolute units by normalizing the integrated intensity of these magnetic reflections by the (110) and (002) nuclear reflections. Using the details of the magnetic structure determined by Bao *et al.* [41] for the parent compound, the results from neutron diffraction for $\mathrm{Ce}_{1-x}\mathrm{Yb}_x\mathrm{RhIn}_5$ were expressed in units of μ_B^2/f.u. and plotted as a function of temperature in Figs. 13(a)–13(c); the resulting intensities show the development of magnetic order as the temperature is cooled below the Néel temperature T_N.

A region of the HHL zone in reciprocal space was mapped using the position-sensitive detector (PSD) for a representative concentration, $x = 0.17$; it is shown in Fig. 13(d). The PSD covers an angular range over five degrees in scattering angle, and hence data were collected for several scattering angles separated by 5°, rotating the crystal in steps on 0.25° over a range of 100°. This measurement was conducted to ensure that no extraneous reflections are present which would suggest additional modifications to the magnetic structure,

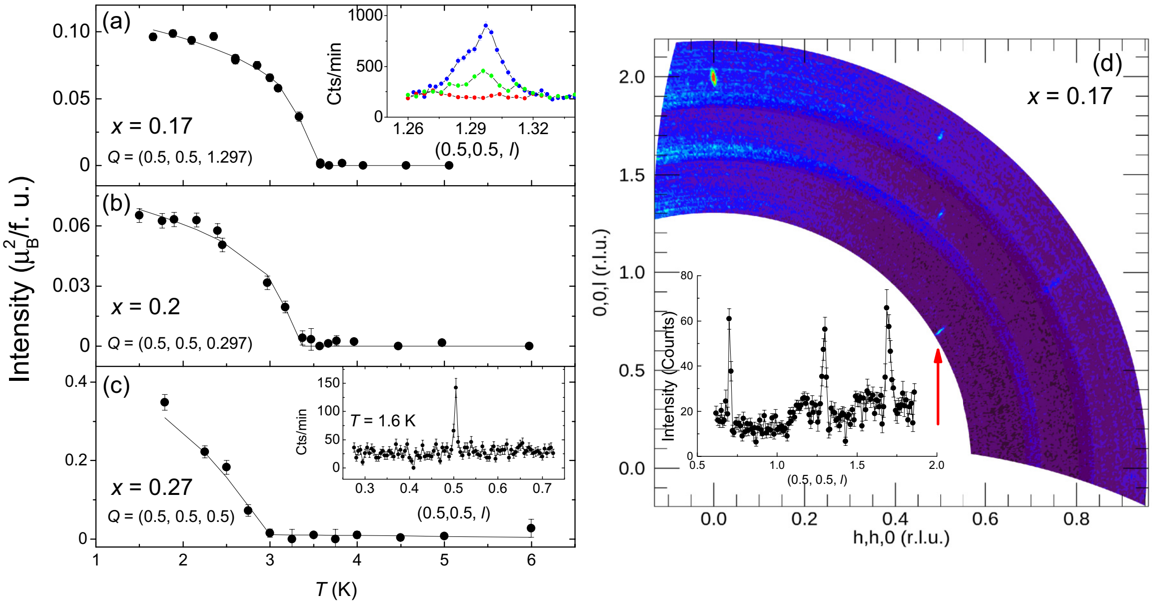

FIG. 13. Neutron diffraction measurements on the BT-4 and BT-7 triple-axis spectrometers at the NIST Center for Neutron Research. (a)–(c) The Néel temperature T_N was determined for concentrations $x = 0.17, 0.2$, and 0.27 by fitting the integrated intensity of a representative magnetic reflection at $Q = G + q$, where G is reciprocal lattice vector, with a mean-field order-parameter function denoted by the solid line. Examples of curves for selected temperatures are shown in the inset of (a), where at the lowest temperature, the peaks were resolution limited. A shoulderlike feature is observed at a slightly lower l; however, no shoulder is observed in scans of the nuclear reflections which indicates a distribution of q values. The inset of panel (c) demonstrates that no evidence for the incommensurate phase was observed for $x = 0.27$ along the (0.5, 0.5, l) direction. (d) A region of the HHL zone in reciprocal space was mapped at 1.5 K for $x = 0.17$. No additional magnetic reflections are present, which would suggest additional modifications to the magnetic structure. The inset of the panel (d), plotted using DAVE [42], shows that, in addition to the bright (110) and (002) nuclear reflections, we observed a series of peaks along (0.5, 0.5, l), which are indexed using the same magnetic propagation vector, q.

relative to that of the parent compound. In addition to the bright (110) and (002) nuclear reflections, we find a series of peaks along the $q = (0.5, 0.5, l)$ vector in the inset of Fig. 13(d). Note that because of the small dimensions of the sample relative to the aluminum sample plate, a substantial background contribution is observed for parts of the map appearing as temperature-independent streaks or peaks of elevated intensity at larger "radii."

The Néel temperatures T_N for $x = 0.17$, 0.20, and 0.27 were extracted by fitting the integrated intensity of a representative magnetic reflection at $Q = G + q$, where G is a reciprocal lattice vector, with a mean-field order-parameter function. The best fits are denoted by the solid lines in Figs. 13(a)–13(c). The ordering temperatures are plotted in Fig. 14(b).

In contrast to the results for the other concentrations, the $x = 0.27$ sample exhibits commensurate order along the unit-cell diagonal described by a propagation vector $q = (0.5, 0.5, 0.5)$. No evidence for the incommensurate phase was observed along the (0.5, 0.5, l) direction as shown in the inset of Fig. 13(c).

For the compound with $x = 0.27$, a second transition T_I below T_N is observed in $C(T)$. However, neutron diffraction measurements show only one transition in this compound, described above as commensurate AFM order at T_N, revealing that T_I is unaccounted for in the neutron diffraction measurements. Possible reasons for this can be that the changes in the magnetic structure below T_I are subtle, or that a different magnetic structure with a distinct propagation vector coexists with the identified commensurate order. Additionally, the inability to detect this potential propagation vector may suggest that the second modulation may have a miniscule magnetic moment. Finally, the transition T_I may be associated with a different phenomenon such as a Lifshitz transition that reflects subtle changes in the electronic density of states. This may be related to changes in the hybridization of conduction- and f-electron states due to the observed valence change.

The difference in magnetic structure for $Ce_{1-x}Yb_xRhIn_5$ between the $x = 0.17$, 0.20, and the 0.27 samples suggests that there is a crossover or transition from incommensurate to commensurate AFM order between $0.20 \leqslant x \leqslant 0.27$, which coincides with changes observed in the behavior of electrical resistivity, magnetic susceptibility, and specific-heat measurements for this concentration range.

IV. CONCLUDING REMARKS

A. Phase diagram

Shown in Figs. 14(a) and 14(b) are the Yb valence v_{Yb} and the Néel temperature T_N vs Yb concentration, respectively. Plots of these v_{Yb} and T_N vs x are shown to emphasize a potential link between the magnetic structure of $Ce_{1-x}Yb_xRhIn_5$ and the valence of Yb. The incommensurate AFM phase appears to correspond to the region over which the Yb valence varies between 3+ and 2.1+, while the commensurate AFM phase appears when the Yb valence becomes stable at 2.1+.

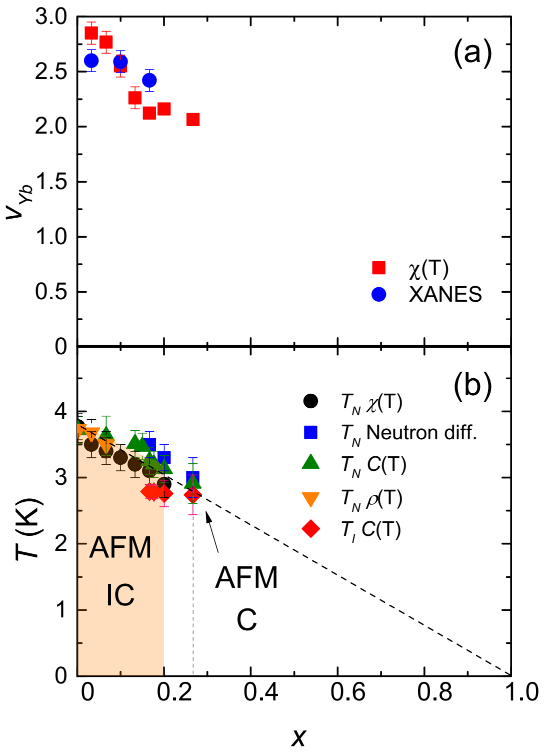

FIG. 14. (a) Yb valence vs Yb concentration x over the same concentration range as the temperature T vs x phase diagram in the panel below. The valence was calculated from magnetic susceptibility measurements with the magnetic field in the *ab* and *c* orientations and from XANES measurements. (b) The T vs x phase diagram for $Ce_{1-x}Yb_xRhIn_5$. The Néel temperature T_N is taken from measurements of the electrical resistivity, magnetic susceptibility, specific heat, and neutron diffraction. A linear fit, indicated by the dashed line, to the $T_N(x)$ data for $Ce_{1-x}Yb_xRhIn_5$ extrapolates to 0 K at $x = 1$. The orange region delineates incommensurate AFM order and the clear region represents commensurate AFM order.

B. Discussion

The phase purity and crystal structures of $Ce_{1-x}Yb_xRhIn_5$ single crystals, synthesized using a molten In flux technique, were confirmed through Rietveld refinement analysis on powder XRD patterns. Given the well-documented subnominal Yb concentrations found in single crystals of the related system $Ce_{1-x}Yb_xCoIn_5$, we determined the actual Yb concentrations in our $Ce_{1-x}Yb_xRhIn_5$ single crystals using EDS and TXAS measurements. Combining the results from these measurements with a Vegard's law analysis of the unit-cell volume as a function of x, we determined that the actual Yb concentrations x_{act} are lower in our $Ce_{1-x}Yb_xRhIn_5$ single crystals than the nominal values x_{nom}. In contrast, results of similar chemical and structural analysis on polycrystalline samples of $Ce_{1-x}Yb_xRhIn_5$ showed $x_{act} \simeq x_{nom}$. Using measurements of magnetic susceptibility and XANES, we estimated the Yb valence as a function of x. Just as has been observed in $Ce_{1-x}Yb_xCoIn_5$, we found that the Yb valence decreases as a function of x until stabilizing at an intermediate valence of 2.1+ near $x = 0.2$. Since the behavior of the valence of $Ce_{1-x}Yb_xRhIn_5$ is similar to that of $Ce_{1-x}Yb_xCoIn_5$, where there is also a Fermi surface reconstruction at $x = 0.07$ indicating an overall change in the electronic structure, it is reasonable to expect a Fermi surface reconstruction at $x = 0.2$ for $Ce_{1-x}Yb_xRhIn_5$. However, additional and difficult types of measurements such as Shubnikov–de Haas would need to be performed to confirm this scenario, although it could potentially provide an explanation for the observed magnetic phase transitions. Neutron scattering experiments demonstrate that the abrupt change in the x dependence of the Yb valence near $x = 0.2$ coincides with a change in the magnetic structure from an incommensurate AFM ground state for $0 \leqslant x \leqslant 0.2$ to a commensurate AFM ground state for $0.2 < x \leqslant 0.27$. Heat-capacity measurements reveal that a second phase transition of magnetic origin emerges in this concentration range at a temperature $T_I < T_N$. Taken together, these results suggest a correlation between the magnetic structure of the heavy-fermion system $Ce_{1-x}Yb_xRhIn_5$ and the intermediate valence of Yb.

ACKNOWLEDGMENTS

Research at UCSD was supported by the Air Force Office of Scientific Research MURI under Grant No. FA9550-09-1-0603 (sample synthesis and screening for superconductivity), the U. S. Department of Energy under Grant No. DE-FG02-04-ER46105 (sample characterization and physical properties measurements), and the National Science Foundation under Grant No. DMR-0802478 (low-temperature measurements). The EXAFS work was supported under NSF Grant No. DMR1005568, and the experiments were performed at Stanford Synchrotron Radiation Lightsource, operated by the U. S. Department of Energy, Division of Chemical Sciences. Support for J.C. was provided by the National Science Foundation under Agreement No. DMR-1508249. The identification of any commercial product or trade name does not imply endorsement or recommendation by the National Institute of Standards and Technology.

---

[1] T. Muramatsu, N. Tateiwa, T. C. Kobayashi, K. Shimizu, K. Amaya, D. Aoki, H. Shishido, Y. Haga, and Y. Onuki, J. Phys. Soc. Jpn. **70**, 3362 (2001).

[2] J. S. Kim, J. Alwood, G. R. Stewart, J. L. Sarrao, and J. D. Thompson, Phys. Rev. B **64**, 134524 (2001).

[3] J. Paglione, M. A. Tanatar, D. G. Hawthorn, E. Boaknin, R. W. Hill, F. Ronning, M. Sutherland, L. Taillefer, C. Petrovic, and P. C. Canfield, Phys. Rev. Lett. **91**, 246405 (2003).

[4] A. Bianchi, R. Movshovich, I. Vekhter, P. G. Paliuso, and J. L. Sarrao, Phys. Rev. Lett. **91**, 257001 (2003).

[5] T. Park, F. Ronning, H. Q. Yuan, M. B. Salamon, R. Movshovich, J. L. Sarrao, and J. D. Thompson, Nature (London) **440**, 65 (2006).

[6] S. Raymond, E. Ressouche, G. Knebel, D. Aoki, and J. Flouquet, J. Phys.: Condens. Matter **19**, 242204 (2007).

[7] G. Knebel, D. Aoki, D. Braithwaite, B. Salce, and J. Flouquet, Phys. Rev. B **74**, 020501(R) (2006).

[8] G. F. Chen, K. Matsubayashi, S. Ban, K. Deguchi, and N. K. Sato, Phys. Rev. Lett. **97**, 017005 (2006).

[9] B. D. White, J. D. Thompson, and M. B. Maple, Phys. C (Amsterdam) **514**, 246 (2015).

[10] W. Bao, P. G. Pagliuso, J. L. Sarrao, J. D. Thompson, Z. Fisk, J. W. Lynn, and R. W. Erwin, Phys. Rev. B **62**, R14621 (2000).

[11] P. Das, S.-Z. Lin, N. J. Ghimire, K. Huang, F. Ronning, E. D. Bauer, J. D. Thompson, C. D. Batista, G. Ehlers, and M. Janoschek, Phys. Rev. Lett. **113**, 246403 (2014).

[12] A. L. Cornelius, P. G. Pagliuso, M. F. Hundley, and J. L. Sarrao, Phys. Rev. B. **64**, 144411 (2001).

[13] D. M. Fobes, S. Zhang, S.-Z. Lin, P. Das, N. Ghimire, E. Bauer, J. Thompson, L. Harriger, G. Ehlers, A. Podlesnyak, R. I. Bewley, A. Sazonov, V. Hutanu, F. Ronning, C. D. Batista, and M. Janoschek, Nat. Phys. **14**, 456 (2018).

[14] F. Ronning, T. Helm, K. R. Shirer, M. D. Bachmann, L. Balicas, M. K. Chan, B. J. Ramshaw, R. D. McDonald, F. F. Balakirev, M. Jaime, E. D. Bauer, and P. J. W. Moll, Nat. Lett. **548**, 313 (2017).

[15] C. Capan, G. Seyfarth, D. Hurt, B. Prevost, S. Roorda, A. Bianchi, and Z. Fisk, Europhys. Lett. **92**, 47004 (2010).

[16] L. Shu, R. E. Baumbach, M. Janoschek, E. Gonzales, K. Huang, T. A. Sayles, J. Paglione, J. O'Brien, J. J. Hamlin, D. A. Zocco, P.-C. Ho, C. A. McElroy, and M. B. Maple, Phys. Rev. Lett. **106**, 156403 (2011).

[17] C. H. Booth, T. Durakiewicz, C. Capan, D. Hurt, A. D. Bianchi, J. J. Joyce, and Z. Fisk, Phys. Rev. B **83**, 235117 (2011).

[18] B. D. White, J. J. Hamlin, K. Huang, L. Shu, I. K. Lum, R. E. Baumbach, M. Janoschek, and M. B. Maple, Phys. Rev. B **86**, 100502 (2012).

[19] Y. P. Singh, D. J. Haney, X. Y. Huang, B. D. White, M. B. Maple, M. Dzero, and C. C. Almasan, Phys. Rev. B **91**, 174506 (2015).

[20] M. Shimozawa, T. Watashige, S. Yasumoto, Y. Mizukami, M. Nakamura, H. Shishido, S. K. Goh, T. Terashima, T. Shibauchi, and Y. Matsuda, Phys. Rev. B **86**, 144526 (2012).

[21] S. Jang, B. D. White, I. K. Lum, H. Kim, M. A. Tanatar, W. E. Straszheim, R. Prozorov, T. Keiber, F. Bridges, L. Shu, and R. E. Baumbach, Philos. Mag. **94**, 4219 (2014).

[22] L. Dudy, J. D. Denlinger, L. Shu, M. Janoschek, J. W. Allen, and M. B. Maple, Phys. Rev. B **88**, 165118 (2013).

[23] A. Polyakov, O. Ignatchik, B. Bergk, K. Götze, A. D. Bianchi, S. Blackburn, B. Prévost, G. Seyfarth, M. Côté, D. Hurt, C. Capan, Z. Fisk, R. G. Goodrich, I. Sheikin, M. Richter, and J. Wosnitza, Phys. Rev. B **85**, 245119 (2012).

[24] T. Hu, Y. P. Singh, L. Shu, M. Janoschek, M. Dzero, M. B. Maple, and C. C. Almasan, Proc. Natl. Acad. Sci. USA **110**, 7160 (2013).

[25] H. Kim, M. A. Tanatar, R. Flint, C. Petrovic, R. Hu, B. D. White, I. K. Lum, M. B. Maple, and R. Prozorov, Phys. Rev. Lett. **114**, 027003 (2015).

[26] Y. Xu, J. K. Dong, I. K. Lum, J. Zhang, X. C. Hong, L. P. He, K. F. Wang, Y. C. Ma, C. Petrovic, M. B. Maple, L. Shu, and S. Y. Li, Phys. Rev. B **93**, 064502 (2016).

[27] V. S. Zapf, N. A. Frederick, K. L. Rogers, K. D. Hof, P.-C. Ho, E. D. Bauer, and M. B. Maple, Phys. Rev. B **67**, 064405 (2003).

[28] V. Zaremba, U. C. Rodewald, R.-D. Hoffmann, Y. M. Kalychak, and R. Poettgen, Z. Anorg. Allgemeine Chem. **629**, 1157 (2003).

[29] J. W. Lynn, Y. Chen, S. Chang, Y. Zhao, S. Chi, W. Ratcliff, II, B. G. Ueland, and R. W. Erwin, J. Res. NIST **117**, 61 (2012).

[30] A. Larson and R. V. Dreele, Los Alamos National Laboratory Report LAUR, No. 86, 2000 (unpublished).

[31] H. M. Rietveld, J. Appl. Crystallogr. **2**, 65 (1969).

[32] W. H. McMaster, N. Kerr Del Grande, J. H. Mallett, and J. H. Hubbell, At. Data Nucl. Data Tables **8**, 443 (1970).

[33] C. MacKeen, F. Bridges, L. Seijo, Z. Barandiarán, M. Kozina, A. Mehta, M. F. Reid, and J.-P. R. Wells, J. Phys. Chem. C **121**, 28435 (2017).

[34] A. D. Christianson, J. M. Lawrence, P. G. Pagliuso, N. O. Moreno, J. L. Sarrao, J. D. Thompson, P. S. Riseborough, S. Kern, E. A. Goremychkin, and A. H. Lacerda, Phys. Rev. B **66**, 193102 (2002).

[35] A. D. Christianson, E. D. Bauer, J. M. Lawrence, P. S. Riseborough, N. O. Moreno, P. G. Pagliuso, J. L. Sarrao, J. D. Thompson, E. A. Goremychkin, F. R. Trouw, M. P. Hehlen, and R. J. McQueeney, Phys. Rev. B **70**, 134505 (2004).

[36] B. E. Light, R. S. Kumar, A. L. Cornelius, P. G. Pagliuso, and J. L. Sarrao, Phys. Rev. B. **69**, 024419 (2004).

[37] J. S. Kim, J. Alwood, D. Mixson, P. Watts, and G. R. Stewart, Phys. Rev. B **66**, 134418 (2002).

[38] T. Willers, F. Strigari, Z. Hu, V. Sessi, N. B. Brookes, E. D. Bauer, J. L. Sarrao, J. D. Thompson, A. Tanaka, S. Wirth, and L. H. Tjeng, Proc. Natl. Acad. Sci. USA **112**, 2384 (2015).

[39] P. J. W. Moll, T. Helm, S.-S. Zhang, C. D. Batista, N. Harrison, R. D. McDonald, L. E. Winter, B. J. Ramshaw, M. K. Chan, F. F. Balakirev, and B. Batlogg, npj Quantum Mater. **2**, 46 (2017).

[40] D. M. Fobes, E. D. Bauer, J. D. Thompson, A. Sazonov, V. Hutanu, S. Zhang, F. Ronning, and M. Janoschek, J. Phys.: Condens. Matter **29**, 17LT01 (2017).

[41] W. Bao, G. Aeppli, J. W. Lynn, P. G. Pagliuso, J. L. Sarrao, M. F. Hundley, J. D. Thompson, and Z. Fisk, Phys. Rev. B **65**, 100505(R) (2002).

[42] R. T. Azuah, L. R. Kneller, Y. Qiu, P. L. W. Tregenna-Piggott, C. M. Brown, J. R. D. Copley, and R. M. Dimeo, J. Res. NIST **114**, 341 (2009).